Elongational Flow-Induced Higher-Order Structure Development in a Supercooled Liquid of a Metallocene-Catalyzed *Syndiotactic* Polystyrene†

Masami Okamoto, Hiroshi Kubo,‡ and Tadao Kotaka*

Advanced Polymeric Materials Engineering, Graduate School of Engineering, Toyota Technological Institute, Hisakata 2-12-1, Tempaku, Nagoya 468-8511, Japan

Received February 9, 1999; Revised Manuscript Received July 13, 1999

ABSTRACT: The development of higher-order crystalline structure induced by uniaxial elongation with constant Hencky strain rates $\dot{\epsilon}_0$ was investigated in the temperature range of 110−140 °C on supercooled liquid of a metallocene-catalyzed *syndiotactic* polystyrene (*s*-PS) via elongational flow opto-rheometry (EFOR), temperature-modulated differential scanning calorimetry, Rayleigh scattering, and polarized Fourier transform infrared spectroscopy. In the elongation at 110 °C where spherulite growth was neglected, chain-segment orientation along the flow preceded and flow-induced crystallization took place rather suddenly at a Hencky strain of $\epsilon(t)$ ($\equiv \dot{\epsilon}_0 t$) $\approx$ 1.2 with the crystalline lamellae irregularly growing transverse to the oriented chains. On the other hand, at 130 °C where spherulite growth was rapid, *strain-induced hardening* due to the spherulite growth was observed in the early stage, and transformation of the spherulites into rodlike morphology followed, accompanying the increasing of birefringence. At 140 °C elongation with a low strain rate of $\dot{\epsilon}_0 = 0.01$ s^{-1}, stable spherulites were formed in the early stage, and the subsequent growth of the spherulites dominated the elongation behavior. However, at 140 °C elongation with high $\dot{\epsilon}_0$ ($\geq$0.1 s^{-1}), formed spherulites were appreciably deformed along the flow direction. Thus, the features of the flow-induced structure development were governed by the dimensionless strain rate that was the ratio of $\dot{\epsilon}_0$ to the spherulite growth rate under the quiescent state. For some semicrystalline polymers, the critical value of the dimensionless strain rate, below/above which the spherulite growth/oriented crystalline formation dominate, increases in order of the decreasing spherulite growth rate, i.e., *s*-PS, poly(ethylene terephthalate), and poly(ethylene naphthalate).

Introduction

In this series of studies,[1−5] we proposed a new method of optical rheometry which enabled us to make simultaneous measurements of transient tensile stress and birefringence on polymeric liquids under uniaxial elongation with constant Hencky strain rates. We called this method *elongational flow opto-rheometry* (EFOR).[1] Then through this new rheometry combined with other ex situ techniques of characterization such as temperature-modulated differential scanning calorimetry (TMDSC) and Rayleigh scattering photometry, we examined elongational rheology[2] and flow-induced structure development[3−5] of poly(ethylene terephthalate) (PET)[2−4] and poly(ethylene naphthalate) (PEN)[5] in their supercooled states that corresponded to blow-molding and/or film-blowing conditions.[6−8] In such studies on elongational flow-induced crystallization of polyesters,[2−5] we demonstrated that a key factor that influenced the crystalline morphology during the elongation was the spherulite growth rate relative to the imposed strain rate. When the former was faster, the spherulite growth preceded the subsequent transformation of grown spherulites into extended and oriented chain crystallites. On the other hand, when the strain rate was faster, the elongation-induced orientation of the chain segments first took place, eventually leading to the oriented crystallite formation. More complex phenomena may be expected by the elongation of extremely rapidly crystallizing polymers, because rapidly grown spherulites may not necessarily be stable ones but may easily be unfolded into extended chain crystallites.

Syndiotactic polystyrene (*s*-PS) prepared with a metallocene catalyst[9] is a semicrystalline polymer having a high stereoregularity, a high melting point of about 270 °C, and a very rapid crystallization rate. In recent years, extensive studies have been carried out on its crystalline morphologies.[10−17] It was found that depending on the crystallization conditions, *s*-PS crystallites may have several different morphologies corresponding to the different chain conformations by Fourier transform infrared (FTIR) spectroscopy.[13−16]

Beside these morphological studies on *s*-PS crystallites developed under quiescent state, Ulcer et al.[17] studied shear-induced crystallization during injection molding, utilizing FTIR, wide-angle X-ray diffraction (WAXD), and differential scanning calorimetry (DSC). They found that the morphologies of the resulting crystallites in the mold were different, depending on the locations they were recovered from, i.e., from the skin layer to the core in the molded specimen, probably reflecting different flow histories such as the local shear rates and temperatures.[17]

However, to our knowledge, there have been no studies so far reported on elongational flow-induced crystallization of *s*-PS. We expect that its rapid spherulite growth rate and its characteristic molecular structure of high stereoregularity may lead to complex elongational flow behavior and development of higher-order crystalline structure. A main objective of this paper is thus to investigate the features of the development of higher-order crystalline structure in *s*-PS induced by elongation. Depending on the flow condi-

* To whom correspondence should be addressed.
† Elongational Flow Opto-Rheometry for Polymeric Liquids. 11.
‡ Present address: Toyoda Boshoku Co., 1-1 Toyoda-cho, Kariya 448-8651, Japan.

10.1021/ma990186q CCC: $18.00
Published on Web 09/03/1999

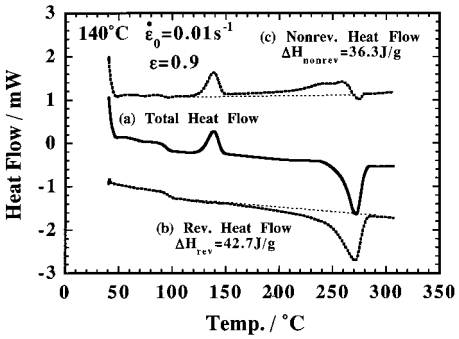

Figure 1. TMDSC scan for a specimen elongated up to $\epsilon = 0.9$ with $\dot{\epsilon}_0 = 0.01$ s^{-1} at 140 °C: (a) total heat flow, (b) reversing heat flow, and (c) nonreversing heat flow.

tions, the spherulites existing before elongation or even those formed in the early stage may transform into a new texture involving an oriented crystalline form. Knowledge of such elongational flow behavior should also be useful in assessing the performance of *s*-PS in processing operations.

Experimental Section

Materials. An amorphous film sample of *syndiotactic* polystyrene (*s*-PS) was supplied by Idemitsu Petrochemical Co. Ltd. The glass transition and melting temperatures were $T_g = 96$ °C and $T_m = 270$ °C, respectively. The weight-average molecular weight was $M_w = 66.5 \times 10^4$, and the polydispersity index, $M_w/M_n = 2.3$, was determined via gel permeation chromatography. Since the as-provided film possessed a slight birefringence on the order of $\sim 5.0 \times 10^{-4}$, we annealed the film to obtain a nonoriented amorphous *s*-PS sheet, first by sandwiching it between polyimide films (KaptonHN, Toray-Dupont) and compression molding it at ~5 MPa with a laboratory hot press kept for 90 s at 300 °C ($> T_m$ of *s*-PS). Then the molded sheet was quickly quenched in ice−water and cut into thin strips of $60 \times 7 \times 0.1$ mm^3 size. The birefringence of the strips before the EFOR measurement was reduced to less than 10^{-5}. These strips were stored at ambient temperature until subjected to EFOR measurements.

EFOR Run. The apparatus[1] was a combination of a Meissner's new elongational rheometer of a metal conveyer belt and gas-cushion type[18] commercialized as Rheometrics Melt Elongational Rheometer (RME, Rheometric Scientific) and a birefringence apparatus of a reflection-double beam path type. We called this modified RME an *elongational flow opto-rheometer* (EFOR)[1] which enabled us to carry out simultaneous measurements of transient tensile stress $\sigma(\dot{\epsilon}_0;t)$ and birefringence $\Delta n(\dot{\epsilon}_0;t)$ as a function of time t under constant tensile strain rate $\dot{\epsilon}_0$. Details were described elsewhere.[1]

On each EFOR run, an amorphous strip was placed in the sample supporting system set at a desired temperature between 110 and 140 °C and annealed for 90 s to reach temperature equilibration before starting the run. The Hencky strain rate $\dot{\epsilon}_0$ was chosen from 0.01 to 1.0 s^{-1}. From transient tensile stress $\sigma(\dot{\epsilon}_0;t)$ data we determined the elongational viscosity $\eta_E(\dot{\epsilon}_0;t)$ ($\equiv \sigma(\dot{\epsilon}_0;t)/\dot{\epsilon}_0$) as a function of $\dot{\epsilon}_0$ and time t. For *s*-PS the birefringence $\Delta n(\dot{\epsilon}_0;t)$ was negative so that absolute values $|\Delta n(\dot{\epsilon}_0;t)|$ were plotted (cf., Figure 6).

TMDSC Run. The glass transition T_g and melting T_m temperatures and the degrees of crystallinity χ_c of the samples were determined on a temperature-modulated differential scanning calorimeter (TMDSC: MDSC, TA2920, TA Instruments) operated at a heating rate of 5 °C/min with a heating/cooling cycle of the modulation period of 60 s and an amplitude of ±0.796 °C.

To estimate the degrees of crystallinity χ_c existing in the test specimens before subjection to DSC analysis, we have to subtract extra heat absorbed by the crystallites formed during the DSC heating process from the total endothermic heat flow due to the melting of the whole crystallites. This can be done by TMDSC. The principles and procedures are found in the relevant literature, for example, by Wunderlich,[19] so that we do not need to recount them here. A brief description of TMDSC applied to PET and PEN was reported in the relevant publications.[2−5]

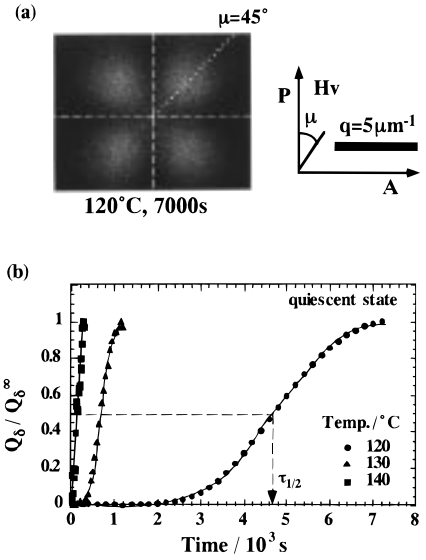

Figure 2. (a) Typical H_v light scattering pattern for 7000s at 120 °C under quiescent state during isothermal crystallization and (b) time variation of reduced invariant Q_δ/Q_δ^∞ during isothermal crystallization at quiescent state in the temperature range from 120 to 140 °C. The arrow indicates the *crystallization half-time* $\tau_{1/2}$ for 120 °C.

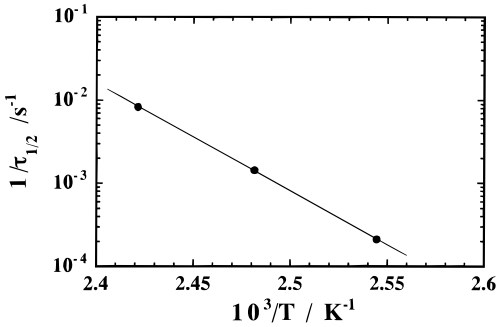

Figure 3. Temperature dependence of the reciprocal half-time of the spherulite growth $1/\tau_{1/2}$.

Figure 1 shows typical TMDSC thermograms in the temperature range 120−290 °C of an *s*-PS specimen elongated up to the Hencky strain ϵ ($\equiv \dot{\epsilon}_0;t$) = 0.9 with the rate $\dot{\epsilon}_0 = 0.01$ s^{-1}. The curve (a) labeled as "Total Heat Flow" is similar to the one obtained on a conventional DSC. On TMDSC the total heat flow profile can be split into (b) "*Reversing* Heat Flow" and (c) "*Nonreversing* Heat Flow". Then the desired endothermic heat flow ΔH_{diff} due to the melting of initially existed crystallites is calculated as $\Delta H_{diff} = \Delta H_{rev} - \Delta H_{nonrev}$, where ΔH_{rev} is the endothermic melting (reversing) enthalpy from the profile (b) for all the crystallites and ΔH_{nonrev}, the exothermic ordering/ crystallization (nonreversing) enthalpy from the profile (c) for the crystallites formed during the DSC heating process. From ΔH_{diff}, the degree of crystallization χ_c was calculated as $\chi_c = \Delta H_{diff}/\Delta H°$, with $\Delta H°$ being the melting enthalpy of 100% crystalline polymer. In this particular case of *s*-PS, the observed enthalpies were $\Delta H_{rev} = 42.7$ J/g and $\Delta H_{nonrev} = 36.3$ J/g. The χ_c was thus $\chi_c = \Delta H_{diff}/\Delta H° = 12.0\%$ with $\Delta H° = 53.2$ J/g of 100% crystalline *s*-PS.[20] The values of χ_c thus estimated are shown later in Figures 6 (in text), 8, and 11.

Rayleigh Scattering Photometry. We employed *time-resolved* light scattering (LS) photometry for estimating the overall crystallization rate and its kinetics in supercooled crystalline polymer liquids under quiescent state.[21−23]

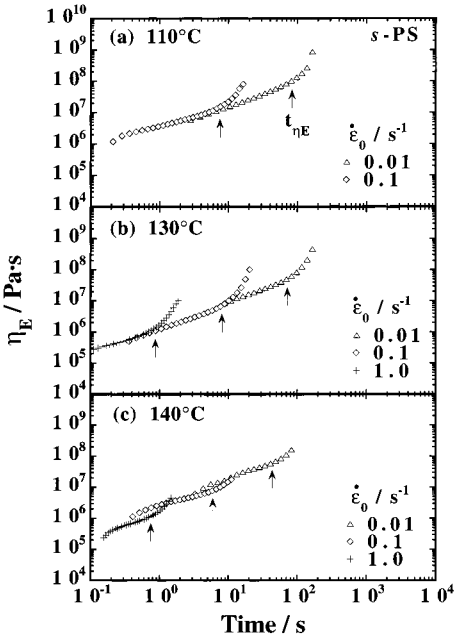

Figure 4. Time variation of elongational viscosity $\eta_E(\dot{\epsilon}_0;t)$ in various supercooled states with various $\dot{\epsilon}_0$ values from 0.01 to 1.0 s^{-1}. The arrows indicate the *up-rising* time $t_{\eta E}$ at which $\eta_E(\dot{\epsilon}_0;t)$ begins to deviate from the linear, $\dot{\epsilon}_0$-independent $\eta_E(\dot{\epsilon}_0;t)$ vs t curves.

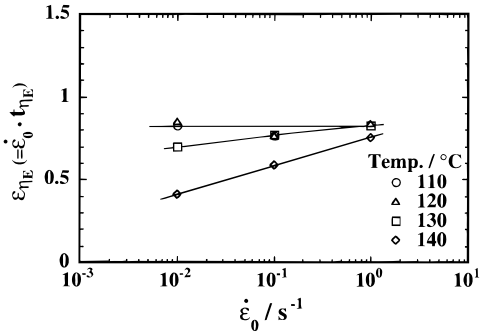

Figure 5. Strain rate $\dot{\epsilon}_0$ dependence of the *up-rising* Hencky strain $\epsilon_{\eta E}$ (=$\dot{\epsilon}_0 t_{\eta E}$) in various supercooled states between 110 and 140 °C.

For the measurement, an *s*-PS film was sandwiched between two pieces of cover glass, placed on a laboratory hot press and compression molded at 300 °C for 90 s to obtain a thin film of about 30−40 μm thick. The molten film was rapidly quenched to a prescribed supercooled state between 110 and 140 °C by putting it on a thermostated hot-stage (Linkam LK600PM, Linkam Scientific Instruments, Ltd.) set on the LS photometer. Immediately after the temperature equilibration, the measurement was carried out as described in the previous articles.[3−5] Usually the scattering profile under H_v (cross-polarized) optical alignment was monitored with PDA and also recorded whenever necessary on a photographic film (Fuji FP-100B; ISO = 100) with an exposure time of 0.25 s.

In the spherulite growth process or isothermal crystallization under quiescent state, scattering intensity $I(q)$ increased with time t, reflecting the increase in optical anisotropy caused by the crystallization. We employed integrated scattering intensity at an azimuthal angle $\mu = 45°$ under the H_v mode, i.e., the invariant Q defined as

$$Q = \int_0^\infty I(q) q^2 \, dq \tag{1a}$$

$$\boldsymbol{q} = (4\pi/\lambda) \sin(\theta_{LS}/2) \tag{1b}$$

where the scattering vector $\boldsymbol{q}$ is defined by eq 1b with

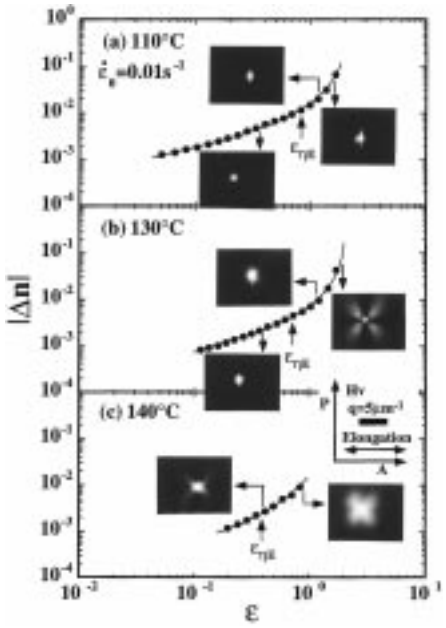

Figure 6. Double logarithmic plots of birefringence $|\Delta n(\dot{\epsilon}_0;t)|$ vs Hencky strain ϵ (=$\dot{\epsilon}_0 t$) and the relevant LS patterns for *s*-PS elongated at (a) 110 °C, (b) 130 °C and (c) 140 °C with $\dot{\epsilon}_0$ = 0.01 s^{-1}.

scattering angle θ_{LS} and wavelength λ of the light in the specimen. For the intensity $I(q)$ of the H_v mode, the invariant Q essentially reflects the optical density fluctuation Q_δ, i.e., the mean-square optical anisotropy $\langle\delta^2\rangle$ defined as

$$Q_\delta \propto \langle\delta^2\rangle \, \phi_s(\alpha_r - \alpha_t)^2 \tag{2}$$

where ϕ_s is the volume fraction of the spherulites and α_r and α_t are the radial and tangental polarizabilities of the crystallites, respectively.[24]

We constructed a plot of reduced invariant Q_δ/Q_δ^∞ vs time t with Q_δ^∞ being Q_δ at an infinitely long time where the crystallization had been completed. For the present case, it was practically ~3 h. Taking the *crystallization half-time* $\tau_{1/2}$ at which Q_δ/Q_δ^∞ reached $^1/_2$, we defined $1/\tau_{1/2}$ as a measure of the *overall* crystallization rate.

We also applied the LS photometry to the specimen recovered after EFOR runs to see the elongational flow-induced crystallization behavior. On the test, a specimen subjected to EFOR to a certain extent of elongation $\epsilon(t)$ ($\equiv\dot{\epsilon}_0 t$) was taken out and quickly quenched by sandwiching it between cold metal plates to freeze the internal structure developed during the elongation.

Polarized Fourier Transform Infrared Spectroscopy. To estimate the orientation factor f_c of crystalline chains developed under elongation, we carried out polarized FTIR spectroscopy on specimens elongated to desired Hencky strains. In such a test, the specimen was quickly quenched by sandwiching it between metal plates, and IR spectra were obtained on an FTIR spectrometer (FT-730, Horiba Ltd.) equipped with a gold wire grid polarizer. The resolution was 0.5 cm^{-1}, and the data accumulation was usually 10 times.

We observed absorbances $A_\parallel$ and $A_\perp$ along the axes parallel and perpendicular to the direction of elongation, respectively. From such spectra we define the dichroic ratio D as the ratio of the absorbances $\bar{A}_\parallel$ and $\bar{A}_\perp$ per unit thickness for a given wavenumber light. In practice, however, instead of directly determining $\bar{A}_i$ (i = || or ⊥), we selected a reference band R with observed absorbances of $A_{i,R}$ (i = || or ⊥), which are independent of the chain conformation,[14] and thus $A_{\perp,R}$, and $A_{\parallel,R}$ approximated the absorbance A_i by the reduced absorbance, $A_i/A_{i,R}$. Thus, the dichroic ratio D is given as

$$D = \frac{\bar{A}_\perp}{\bar{A}_\parallel} \cong \frac{A_\perp/A_{\perp,R}}{A_\parallel/A_{\parallel,R}} \tag{3}$$

Then from D for the orientation sensitive band, we determine the orientation factor f as

$$f = \frac{2}{(3\cos^2\gamma - 1)} \cdot \frac{1 - D}{1 + 2D} \tag{4}$$

where γ is the angle between the dipole-moment vector of vibration and the chain axis. The orientation factor f can also be defined by

$$f = \frac{3\langle\cos^2\theta\rangle - 1}{2} \tag{5}$$

as the second moment of the distribution of angle θ that is the angle between the chain axis and the stretching direction.

Results

Rayleigh Scattering Photometry under a Quiescent State. Figure 2a shows a typical example of light-scattering H_v-pattern for *s*-PS under a quiescent state at 120 °C after a sufficiently long time (~7000 s), by which time the spherulite growth had been nearly completed and the spherulites covered the entire field of an optical microscope. In Figure 2a, we observe a four-leaf-clover pattern with an azimuthal angle $\mu = 45°$ typical for well-developed spherulites, but the locations and intensities of the scattering maxima along the azimuthal angle μ are not quite clear. Thus, from time evolution of the peak angles and intensities, we could not determine the average spherulite size. We then followed time-evolution of the reduced invariant Q_δ/Q_δ^∞. Figure 2b shows examples of Q_δ/Q_δ^∞ *vs t* curves at three different temperatures from 120 to 140 °C. In Figure 3, we constructed an Arrhenius plot of the *crystallization half time* $\tau_{1/2}$ against reciprocal temperature $1/T$ for their spherulite growth behavior. From the slope the apparent activation energy is estimated to be about 6.1 kJ/mol for the spherulite growth. This value is comparable to the value of ~6.5 kJ/mol reported for *isotactic* PS.[25]

Elongational Viscosity. We then determined on EFOR transient tensile stress $\sigma(\dot{\epsilon}_0;t)$ and elongational viscosity $\eta_E(\dot{\epsilon}_0;t)$ ($\equiv\sigma(\dot{\epsilon}_0;t)/\dot{\epsilon}_0$) for *s*-PS as a function of $\dot{\epsilon}_0$ and t in the temperature range between 110 and 140 °C. Figure 4 shows the results. The arrows in the figures show the critical (*up-rising*) time $t_{\eta E}$ at which upward deviation of $\eta_E(\dot{\epsilon}_0;t)$ from the $\dot{\epsilon}_0$-independent portion becomes prevailing. We often call the $\dot{\epsilon}_0$-independent portion the *linear* portion and call the upward deviation *strain-induced hardening*.[26] We see that the curves with $\dot{\epsilon}_0 = 0.1-1.0\ s^{-1}$ at 110 and 130 °C possess a linear portion, while the curve at 140 °C appears to have no linear portion.

In Figure 5 we plotted the critical (up-rising) Hencky strain $\epsilon_{\eta E}$ ($\equiv\dot{\epsilon}_0 t_{\eta E}$) against the Hencky strain rate $\dot{\epsilon}_0$. We see quite a different behavior of $\epsilon_{\eta E}$ vs $\dot{\epsilon}_0$ between the 110−120 °C range and the 130−140 °C range. In the 110−120 °C elongation, $\epsilon_{\eta E}$ remains almost constant around 0.8, and in the 130 °C elongation, $\epsilon_{\eta E}$ only slightly decreases with decreasing $\dot{\epsilon}_0$ (=0.01 s^{-1}), whereas in the 140 °C elongation, $\epsilon_{\eta E}$ decreases rather rapidly.

Changes in Birefringence and Scattering Patterns Induced by Elongation. Figure 6 shows $|\Delta n(\dot{\epsilon}_0;t)|$ vs ϵ ($\equiv\dot{\epsilon}_0 t$) curves obtained at 110−140 °C for *s*-PS elongated with $\dot{\epsilon}_0 = 0.01\ s^{-1}$. Relevant Rayleigh scattering patterns are shown in the figure at several locations indicated with the arrows. As seen in Figure 6a, the specimen elongated at 110 °C up to $\epsilon \cong 0.36$ (where $\chi_c \cong 0.8$ wt %) exhibits only a weak scattering pattern without anisotropy. However, beyond $\epsilon \cong 1.64$, the LS pattern suddenly begins to exhibit streaks along the meridional direction perpendicular to the stretch direction, suggesting that strong molecular orientation in the real space has proceeded along the direction of elongation. Around $\epsilon \cong 1.64$, the degree of crystallinity χ_c jumps up to 20.3 wt %, but the specimen exhibits no stress-*whitening*. The increase in χ_c is an indication of the elongational flow-induced oriented crystallite formation. However, as opposed to the elongation of PET (with low $\dot{\epsilon}_0$ (=0.01 s^{-1}) at a low temperature (T_g + 34 °C) which showed strong two spot-patterns due to ordered crystalline lamella[3], in *s*-PS at 110 °C we see no two-spot pattern in the direction parallel to the stretch direction. These results imply that the crystalline texture in *s*-PS is disordered, as opposed to the elongation of PET.

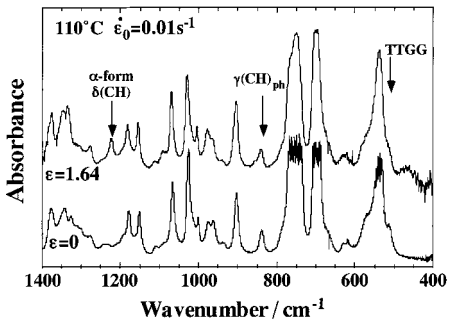

Figure 7. FTIR spectra taken from a specimen before ($\epsilon = 0$) and after elongation with $\dot{\epsilon}_0 = 0.01 s^{-1}$ up to $\epsilon = 1.64$.

Figure 6b shows similar data for *s*-PS elongated at 130 °C. The specimen elongated up to $\epsilon \cong 0.39$ also exhibits a weak scattering pattern without anisotropy similar to that elongated at 110 °C up to $\epsilon \cong 0.36$. The specimen begins to exhibit a weak lobelike pattern at $\epsilon \cong 0.39$ (where $\chi_c \cong 30$ wt %), and clearer lobelike pattern[25,4,5] (but without streaks along the meridional direction perpendicular to the stretch direction) at $\epsilon \cong 1.94$ (where $\chi_c \cong 21.0$ wt %).

Quite different LS patterns are seen for *s*-PS elongated at 140 °C as shown in Figure 6c. At $\epsilon \cong 0.40$, just above the *up-rising* strain $\epsilon_{\eta E} \cong 0.38$, the specimen exhibits a weak smeared four-leaf-clover pattern ($\chi_c \cong$ 4.0 wt %) and that elongated up to $\epsilon \cong 0.91$ exhibits a further smeared pattern, implying spherulite deformation or break down has taken place (where $\chi_c \cong 12.0$ wt %). The crystallization behavior at 140 °C elongation is entirely different from that at 110 or 130 °C elongation. In the former, the spherulite growth dominates especially in those elongated with low $\dot{\epsilon}_0$ (<0.1 s^{-1}) and the critical Hencky strain $\epsilon_{\eta E}$ is strongly dependent on $\dot{\epsilon}_0$, as seen in Figure 5.

Orientation of *s*-PS Crystallites Developed under Elongation. First, Figure 7 shows nonpolarized FTIR spectra in the range 400−1400 cm^{-1} obtained for an unelongated *s*-PS specimen ($\epsilon = 0$) annealed at 110 °C for 90 s and that elongated at 110 °C up to $\epsilon \cong 1.64$ with $\dot{\epsilon}_0 = 0.01\ s^{-1}$.

The 1224 cm^{-1} band was assigned as the methine CH deformation (δ(CH)) characteristic of α-form crystallites, but does not exist in the amorphous *s*-PS specimen.[15] The absorbance of the 1224 cm^{-1} band thus reflects the

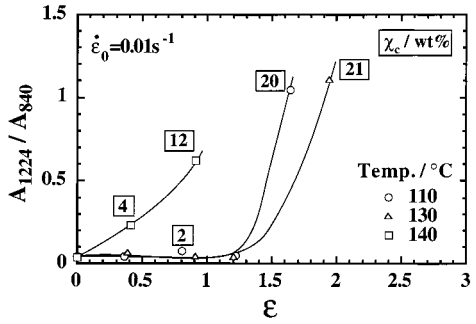

Figure 8. Reduced absorbance of the 1224 cm^{-1} band vs Hencky strain ϵ (=$\dot{\epsilon}_0 t$) elongated with $\dot{\epsilon}_0 = 0.01\ s^{-1}$ at various temperature. The degree of % crystallinity χ_c of each specimen was shown with the number in the box.

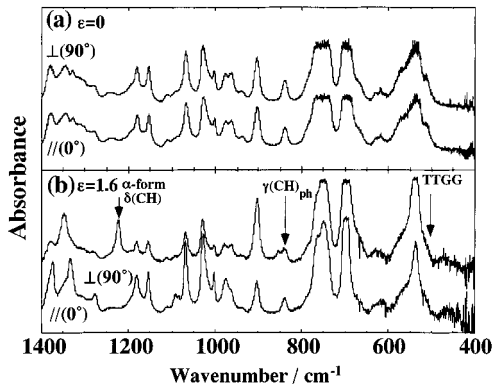

Figure 9. Polarized FTIR spectra for perpendicular (⊥) and parallel (||) to the stretch direction of (a) before and (b) after elongation for up to $\epsilon = 1.64$ with $\dot{\epsilon}_0 = 0.01\ s^{-1}$ at 110 °C.

crystalline content. On the other hand, the 840 cm^{-1} band is a conformation-independent band corresponding to out-of-plane deformation of CH in phenyl ring (γ-$(CH)_{ph}$)[14,15] and can be taken as the reference band. Thus, for *s*-PS the ratios of the 1224 cm^{-1} band to the 840 cm^{-1} band reflect the degrees of crystallinity χ_c.

In Figure 8, the reduced absorbances A_{1224}/A_{840} are plotted as a function of $\epsilon(t)(\equiv \dot{\epsilon}_0 t)$ together with the values of χ_c determined from the TMDSC analyses for *s*-PS specimens elongated at 110−140 °C with $\dot{\epsilon}_0 = 0.01\ s^{-1}$ up to various extent of elongation. At 110 and 130 °C the specimens hardly show increase in χ_c until $\epsilon \cong 1.2$, beyond which they exhibit a rapid increase in χ_c, indicating that the elongational flow-induced crystallization has taken place. However, at 140 °C the reduced absorbance A_{1224}/A_{840} shows gradual increase with ϵ from the very beginning of elongation. This suggests that at 140 °C the spherulite growth is dominant because of its high spherulite growth rate.

Next, we carried out polarized FTIR measurement on the same specimens to see the features of the flow-induced orientation. Figure 9 compares polarized FTIR spectra in the range of 400 to 1400 cm^{-1} for the specimen (a) before elongation ($\epsilon = 0$) annealed at 110 °C for 90 s and (b) that elongated up to $\epsilon \cong 1.64$ at 110 °C with $\dot{\epsilon}_0 = 0.01\ s^{-1}$. Both panels include two spectra, one for perpendicular (⊥) to and the other parallel (||) to the stretch direction. The two spectra are the same for the unelongated specimen ($\epsilon = 0$), but they are quite different for that elongated up to $\epsilon \cong 1.64$. Particularly, for the 1224 cm^{-1} band assigned to α-form crystalline domain, the absorbance of the perpendicular (⊥) direction is quite strong, whereas that in the parallel (||) direction is weak. This behavior was reported previously

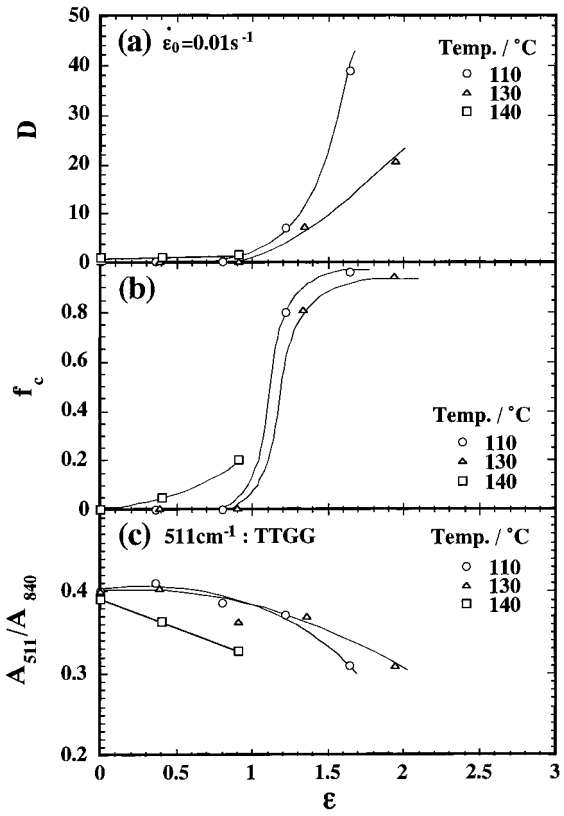

Figure 10. Plots of (a) dichroic ratio *D*, (b) orientation function of crystalline chain f_c, and (c) TTGG component vs Hencky strain ϵ at various supercooled state.

by Kobayashi et al. on an oriented *s*-PS specimen.[15]

We determined dichroic ratio (*D*) and calculated orientation factor (f_c) for the 1224 cm^{-1} band by using eqs 3 and 4 with assumption of $\gamma = 90°$. Figure 10 shows the results of (a) *D* and (b) f_c of the α-form crystalline domain thus estimated from the 1224 cm^{-1} band. The figure also includes (c) the ratio of the absorbance A_{511}/A_{840}, which reflects the proportion of trans−trans−gauche−gauche (TTGG) conformation, which is in turn related to the amorphous content. [15]

For *s*-PS specimens, Figure 10a shows that the value of *D* is nearly zero up to $\epsilon \cong 1.0$, beyond which, especially under 110 °C elongation, the value of *D* rapidly increases with ϵ corresponding to the rapid increase in χ_c (cf., Figure 8). Under 140 °C elongation, however, the specimen cannot be elongated beyond $\epsilon \cong 1.0$ and does not show any indication of net increase in the orientation of the crystallites, although χ_c steadily increases to 12 wt % at $\epsilon \cong 1.0$. These results imply that in the former case of 110−130 °C elongation, the crystallites are not yet formed at all below $\epsilon \cong 1.0$, but the orientation of the crystalline chains as well as the crystallization itself are encouraged around $\epsilon \cong 1.6$−1.9, resulting in the formation of oriented chain crystallites. On the other hand, at 140 °C elongation, spherulite growth is dominant, leading to a steady increase in χ_c but no net increase in chain orientation.

This situation is more clearly seen in Figure 10b, where for both 110 and 130 °C elongation f_c starts to increase at around $\epsilon \cong 1.0$, increases more rapidly beyond $\epsilon \cong 1.2$, and finally reaches a near perfect orientation of $f_c \cong 0.95$. On the other hand, at 140 °C, f_c increases rather slowly with ϵ and reaches only 0.2 at $\epsilon \cong 0.91$, regardless of χ_c reaching 12 wt %.

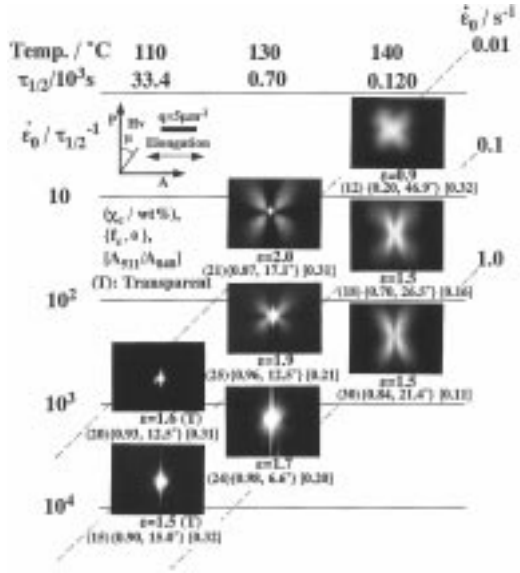

Figure 11. Changes in H_v scattering patterns at ultimate elongation and the corresponding data of χ_c, f_c, and θ and TTGG components for various elongation temperatures and $\dot{\epsilon}_0$ values. Each H_v pattern is located on the dimensionless Hencky strain ($\dot{\epsilon}_0/\tau_{1/2}^{-1}$) vs elongation temperature map.

As shown in Figure 10c by A_{511}/A_{840} for the 511 and 840 cm^{-1} bands, we see that the TTGG component monotonically decreases with ϵ at 140 °C, because of the spherulite growth, which leads to dominantly all trans (TTTT) conformation. However, at both 110 and 130 °C, the TTGG component first stays constant but later decreases steadily, implying that the *s*-PS chain conformation changes to favor the *trans*-type in elongational flow.

Discussion

Higher-Order Crystalline Structure Development under Elongation. In Figure 11, we summarize the LS patterns obtained from the specimens elongated to certain extent at three different temperatures and strain rates $\dot{\epsilon}_0$ together with the values of χ_c, f_c, and θ (calculated by eq 5) and the TTGG component of the specimens. As already seen in Figure 8, the crystallization behaviors at 110 and 130 °C as revealed by χ_c vs ϵ relations seem to resemble each other. However, the specimen elongated at 110 °C remains transparent even at $\epsilon \cong 1.64$ where χ_c ($\cong$ 20 wt %) is considerably higher, while that at 130 °C exhibits significant *whitening* beyond $\epsilon \cong 1.98$. The specimen elongated at 140 °C undergoes whitening as strong as those at 130 °C from a very early stage.

The LS patterns also suggest that the crystalline textures are different among those elongated under different conditions. For the specimen elongated at 110 °C, the LS pattern exhibits only strong streaks perpendicular to the elongation, suggesting that the elongational flow-induced oriented crystalline formation has taken place. Similar scattering patterns were observed under a depolarized optical alignment of the V_v mode. On the other hand, for those elongated at 130 °C, the LS patterns are different depending on $\dot{\epsilon}_0$, suggesting that the strain rates also may influence the crystalline textures. The specimen elongated with low $\dot{\epsilon}_0$ (=1 s^{-1}) up to $\epsilon \cong 1.98$ shows a rodlike pattern without streaks, whereas that with high $\dot{\epsilon}_0$ (=1.0 s^{-1}) exhibits clear and strong streaks in the direction perpendicular to the stretch direction. For those elongated at 140 °C, where the spherulite growth is very fast, spherulites continue to develop even under elongation. Under such a condition, a four-leaf-clover pattern typical of the spherulites becomes more and more deformed with increasing $\dot{\epsilon}_0$. In fact, Figure 11 suggests that under 140 °C elongation the higher the strain rate is, the more enhanced is the spherulite deformation, as revealed by the decrease in the azimuthal angle μ of the four-leaf-clover pattern from nearly 45 to 20° as the rate $\dot{\epsilon}_0$ is increased from 0.01 to 1.0 s^{-1} with f_c increasing from 0.20 to 0.84.

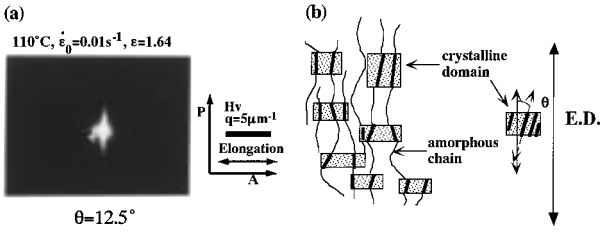

Figure 12. (a) Typical H_v scattering pattern for *s*-PS elongated at 110 °C with ($\dot{\epsilon}_0/\tau_{1/2}^{-1}$) = 0.01 s^{-1} up to $\epsilon = 1.64$. (b) Model of the crystalline texture. The angle θ is associated with the average orientation angle of the crystalline chain axis.

As a plausible interpretation of these patterns, we propose the following models for higher-order crystalline textures developed under elongation, as shown in Figures 12−14. Figure 12 shows, for a specimen elongated at 110 °C with $\dot{\epsilon}_0 = 0.01$ s^{-1} up to $\epsilon = 1.64$, (a) an enlarged LS pattern and (b) a crystalline texture model. The model implies that the crystalline texture (lamellae) grows normal to the oriented chains without regularity. In such a case of low-temperature elongation, the flow-induced oriented crystalline formation overwhelms the slow spherulite growth. The chains are first oriented along the direction of elongation until ϵ exceeds 1. Then lamellae develop in the direction perpendicular to the stretch direction and end up at $\epsilon = 1.64$ with the average orientation angle of the chain axes $\theta = 12.5°$, as depicted in Figure 12b.

For the elongation at 130 °C, the spherulites developed before and/or in the early stage of elongation deform and eventually transform into new crystalline morphologies depending on the competition between spherulite growth and strain rate. The effect of strain rate $\dot{\epsilon}_0$ on elongational flow-induced crystallization is more obvious for the specimens elongated at 130 °C, where the spherulite growth rate is appreciable, as opposed to the 110 °C elongation. Figure 13a is an enlarged photograph of the LS pattern of the specimen elongated at 130 °C with a low strain rate $\dot{\epsilon}_0 = 0.01$ s^{-1} up to $\epsilon \cong 1.98$. Generally oriented crystallites are expected to show a pattern consisting of two parts: One is two split streaks inclined with an angle α, and the other is two diffuse lobes inclined with an angle β to the direction of elongation, such as is schematically shown in Figure 13b.[27] According to Yau and Stein,[27] the former corresponds to the inclination of rodlike texture composed of stacked lamellae, while the latter corresponds to the inclination of the lamellae themselves. In the present case shown in Figure 13a; however, we can barely see the streaks form the rods with an inclination α but can clearly see the lobes with inclination β of 45°. Figure 13c depicts a morphology model. The average orientation angle of the stretched chains is $\theta = 17.1°$ as revealed by polarized FTIR analysis.

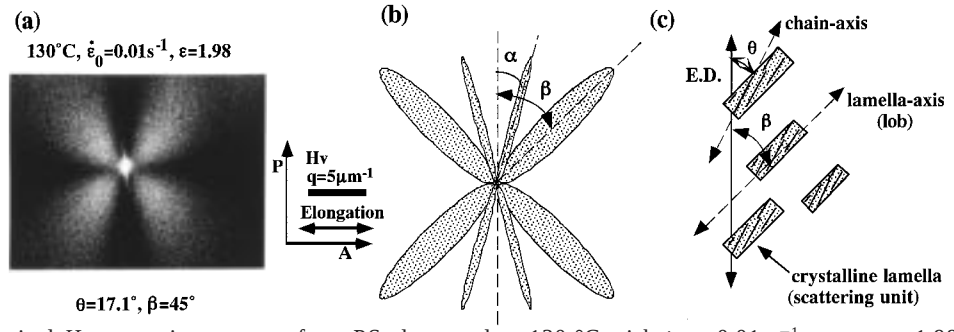

Figure 13. (a) Typical H_v scattering pattern for *s*-PS elongated at 130 °C with $\dot{\epsilon}_0 = 0.01$ s^{-1} up to $\epsilon = 1.98$, (b) its schematic representation, and (c) a model describing the arrangement of rodlike texture with respect to the elongational direction (E.D.). The angles α, β, and θ are associated with the average orientation angle of the rods (the assembly of the lamellae) and that of the lamella axis and the crystalline chain axis, respectively, as depicted in the model.

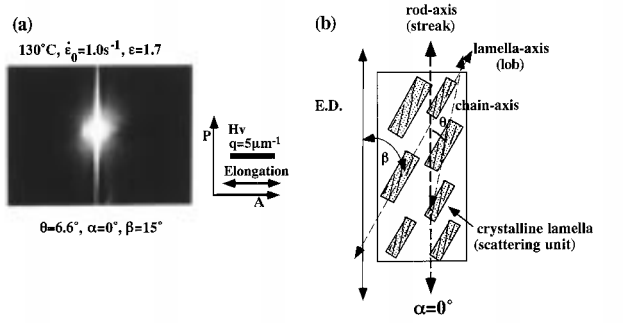

Figure 14. (a) Typical H_v scattering pattern for *s*-PS elongated at 130 °C with $\dot{\epsilon}_0 = 1.0$ s^{-1} up to $\epsilon = 1.7$. (b) Model describing the arrangement of rodlike texture with respect to the elongational direction (E.D.). The angles α, β, and θ are associated with the average orientation angle of the rods (the assembly of the lamellae) and that of the lamella axis and the crystalline chain axis, respectively, as depicted in the model.

On the other hand, Figure 14a shows an enlarged LS pattern for a specimen elongated at 130 °C with a high strain rate $\dot{\epsilon}_0 = 1.0$ s^{-1} up to $\epsilon \cong 1.70$. Strong streaks arise from the rods of stacked crystalline lamellae with inclination α ($\cong$ 0) that are almost parallel to the direction of elongation so that two streaks merge into one, while thin lobes arise from the lamellae themselves with inclinaton $\beta \sim 15°$ to the direction of elongation. The value of $\theta = 6.6°$ is much less than that for low $\dot{\epsilon}_0$ elongation. We see that the higher $\dot{\epsilon}_0$ is, the more encouraged is the formation and orientation of the rods accompanying more intense chain orientation.

Strain-Induced Hardening vs Crystallization Behavior. As discussed in our previous papers on PET and PEN,[4] in the case of supercooled *s*-PS liquids, the spherulite growth rate is also a key factor governing the elongational rheology. Generally spherulite growth leads to an enhancement in $\sigma(\dot{\epsilon}_0;t)$ and thus in $\eta_E(\dot{\epsilon}_0;t)$ to an extent larger than that expected from the viscoelastic stress contribution. For *s*-PS at 140 °C in which spherulite growth is rapid (cf., Figure 2), we recognize that the critical Hencky strain $\epsilon_{\eta E}$ ($\equiv \dot{\epsilon}_0 t_{\eta E}$) for the onset of strain-induced hardening is strongly $\dot{\epsilon}_0$-dependent. Using the reciprocal of *crystallization half-time*, $1/\tau_{1/2}$, as defined in Figure 2 for the overall crystallization rate, we reconstructed *reduced* plots of $\epsilon_{\eta E}$ vs $\dot{\epsilon}_0 \cdot \tau_{1/2}$ from the $\epsilon_{\eta E}$ vs $\dot{\epsilon}_0$ data of Figure 5. The results are shown in Figure 15.

We see that all the data nicely conform to a *reduced* curve with $\epsilon_{\eta E} \cong 0.8$ for the dimensionless Hencky strain rate $\dot{\epsilon}_0\tau_{1/2} > 50$, whereas $\epsilon_{\eta E}$ approaches zero as $\dot{\epsilon}_0\tau_{1/2}$ is decreased well below 50. The critical strain rate $(\dot{\epsilon}_0\tau_{1/2})_c$ is thus $\cong$50, above which oriented crystallite formation

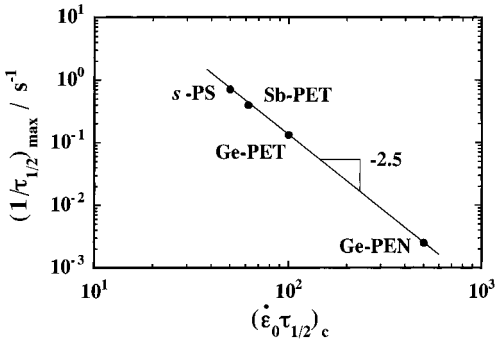

Figure 15. Reduced plots of $\epsilon_{\eta E}$ vs $(\dot{\epsilon}_0\tau_{1/2})$ for *s*-PS elongated at various temperatures. The arrow indicates the critical (dimensionless) Hencky strain $(\dot{\epsilon}_0\tau_{1/2})_c$ ($\cong$50).

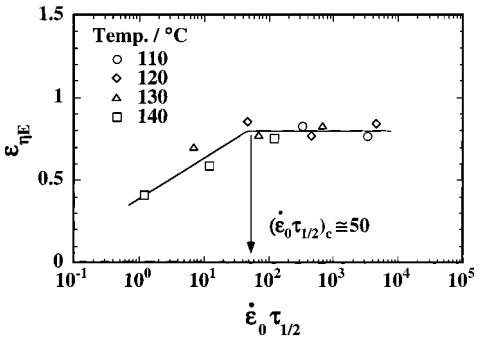

Figure 16. Plot of maximum reciprocal half-time of the spherulite growth $(1/\tau_{1/2})_{max}$ vs critical dimensionless Hencky strain $(\dot{\epsilon}_0\tau_{1/2})_c$ for *s*-PS, Sb−PET, Ge−PET, and Ge−PEN.

and/or the transformation of spherulites into oriented crystallites prevail. In the elongation of *s*-PS with a high $\dot{\epsilon}_0\tau_{1/2}$ (>50), elongational flow-induced oriented crystallite formation is overwhelming, and otherwise the spherulite growth dominates the *strain-induced hardening* behavior.

This value, $(\dot{\epsilon}_0\tau_{1/2})_c$, of ~50 is comparable to that of Sb-catalyzed PET (Sb−PET).[4] The value is half of that of Ge-catalyzed PET (Ge−PET) ($\cong$100)[4] and one-tenth of that for Ge−PEN (500).[5] Figure 16 compares the $(\dot{\epsilon}_0\tau_{1/2})_c$ value vs the maximum value of $1/\tau_{1/2}$, which is estimated at the middle point between T_g and T_m^0 (being the equilibrium melting temperature of 310 °C[28] for s-PS, 280 °C,[23] for PET and 300 °C[29] for PEN) of the spherulite growth rate vs T curve. Interestingly, a strong negative correlation is seen between $(1/\tau_{1/2})_{max}$ and $(\dot{\epsilon}_0\tau_{1/2})_c$ for three different polymers. This means that the faster the spherulite growth is, the easier is the transformation into oriented crystallites. This relation may be important in optimizing processing condi-

tions (e.g., blow-molding) of each resin to obtain a transparent material containing the smallest amount of spherulites. Note the smaller value of $(\dot{\epsilon}_0\tau_{1/2})_c$ for *s*-PS as compared with others, implying that deformation of crystallized *s*-PS molecules takes place easily, presumably because of the absence of rigid units in the backbone such as phenyl and/or naphthalene rings.

Conclusions

We examined the features of elongational flow-induced higher-order structure development in *s*-PS in the temperature range 110−140 °C where the spherulite growth rate is highly temperature-dependent. In the case of slowly crystallizing *s*-PS elongated at 110 °C, flow-induced orientation of the amorphous chain segments took place until a Hencky strain $\epsilon \cong 1.2$ being reached, beyond which oriented crystalline formation with disordered crystalline texture became prevailing, as revealed by the LS pattern, polarized FTIR, and TMDSC.

At 130 °C, rather rapid growth of spherulites but with low stability dominated in the early to middle stage of the elongation, and later beyond $\epsilon \geq 1.2$, transformation to a new crystalline texture, i.e., the rodlike crystalline morphology, follows.

On the other hand, at 140 °C, especially with a low strain rate $\dot{\epsilon}_0 = 0.01\ s^{-1}$ where the spherulite growth is very rapid, crystallization leads to strong *strain-induced hardening* in $\sigma(\dot{\epsilon}_0;t)$ vs t profiles and subsequent reduction in $|C(\dot{\epsilon}_0;t)|$ reflects an increasing of $\sigma(\dot{\epsilon}_0;t)$ (see Appendix, Figure 17) but a rather weak enhancement in $\Delta n(\dot{\epsilon}_0;t)$ due to the nondeformation of the spherulite in the beginning of the elongation. However, with high $\dot{\epsilon}_0 = 0.1-1.0\ s^{-1}$ the spherulites are forced to deform toward the direction of elongation accompanying the increase in the orientation function of the crystalline chains.

Thus, the flow-induced oriented crystalline formation and the spherulite growth are competing process in the elongational flow of supercooled *s*-PS. Beside the magnitude of the strain rate relative to the spherulite growth rate, an additional factor governing the crystallization behavior is the stability or the deformability of the spherulites grown in the early stage. If the grown spherulites are unstable, they eventually undergo deformation and transformation into flow-induced oriented crystallites when stretched with high $\dot{\epsilon}_0$.

Acknowledgment. We wish to thank Dr. T. Takebe of Idemistu Petrochemical Co. Ltd. for kindly providing the *s*-PS sample.

Appendix. Stress Optical Rule for *s*-PS Supercooled Liquids under Elongation

For uniaxial elongation of polymer melt the stress optical rule[30,31] simply reads as follows:

$$\Delta n(\dot{\epsilon}_0;t) = C(\dot{\epsilon}_0;t)\cdot\sigma(\dot{\epsilon}_0;t) \qquad \text{(A1)}$$

The stress optical coefficient $C(\dot{\epsilon}_0;t) = \Delta n(\dot{\epsilon}_0;t)/\sigma(\dot{\epsilon}_0;t)$, first given by Treloar et al.[32,33] for rubber elasticity, is supposed to be independent either of time t, strain ϵ, tensile stress σ or strain rate $\dot{\epsilon}_0$. Figure 17 compares the three $C(\dot{\epsilon}_0;t)$ vs $\sigma(\dot{\epsilon}_0;t)$ curves for the supercooled *s*-PS liquids elongated at 110, 130, and 140 °C all with $\dot{\epsilon}_0 = 0.01\ s^{-1}$.

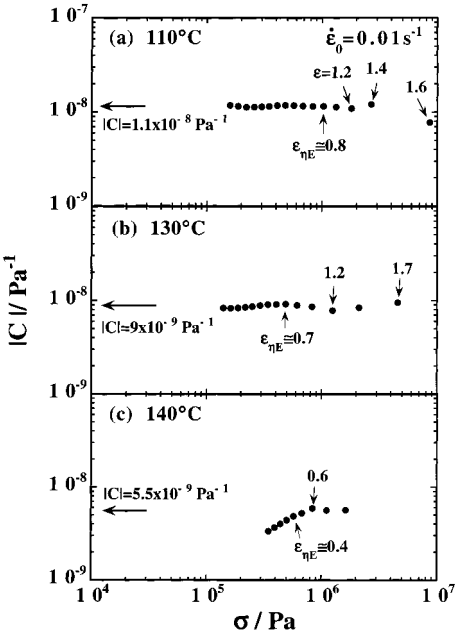

Figure 17. Double logarithmic plots of stress optical coefficient $|C(\dot{\epsilon}_0;t)| = |\Delta n(\dot{\epsilon}_0;t)|/\sigma(\dot{\epsilon}_0;t)$ vs tensile stress $\sigma(\dot{\epsilon}_0;t)$ for *s*-PS elongated with $\dot{\epsilon}_0 = 0.01\ s^{-1}$ at various temperatures.

At 110 °C, the value of $|C(\dot{\epsilon}_0;t)|$ is constant ($\cong 1.1 \times 10^{-8}$ Pa^{-1}) in the early stages up to $\sigma(\dot{\epsilon}_0;t) \cong 2$ MPa ($\epsilon \cong 1.2$), indicating that the stress optical rule is obeyed but the value is twice as large as that for *atactic* PS elongation.[1] According to the very recent study of Ryu et al.,[34] a plausible interpretation for $|C(\dot{\epsilon}_0;t)|$ is the effect of the different tacticity on the molecular stiffness. Beyond the stress $\sigma(\dot{\epsilon}_0;t) \cong 2$ MPa, the value of $|C(\dot{\epsilon}_0;t)|$ deviates once more upward and then to downward. The upward deviation indicates the start of the orientation crystallization, which has a larger intrinsic birefringence and a higher degree of orientation than the amorphous region. The following downward deviation is due to a rapid increase of $\sigma(\dot{\epsilon}_0;t)$ caused by the prevailing crystal growth as shown in Figure 8.

At 130 °C, the early $|C(\dot{\epsilon}_0;t)|$ value ($\cong 0.9 \times 10^{-8}$ Pa^{-1}) is slightly smaller than that of 110 °C. Since, at 130 °C, the spherulite growth rate is faster than that at 110 °C, the effect of the spherulite growth on $\sigma(\dot{\epsilon}_0;t)$ affects the beginning stage of elongation. The upward deviation starts beyond $\sigma(\dot{\epsilon}_0;t) \cong 1.2$ MPa ($\epsilon \cong 1.2$) and the downward deviation such as is observed at 110 °C is not seen in the late stage of elongation. The upward deviation of $|C(\dot{\epsilon}_0;t)|$ appears to take the place of the transformation of the spherulite into rodlike crystalline texture, where the excess $\Delta n(\dot{\epsilon}_0;t)$ over applied $\sigma(\dot{\epsilon}_0;t)$ might prevail due to the crystallized chain reorientation.

On the other hand, at 140 °C, where the crystal growth rate is so rapid, the value of $|C(\dot{\epsilon}_0;t)|$ exhibits quite a different behavior compared with both 110 and 130 °C behaviors. The strong downward deviation of $|C(\dot{\epsilon}_0;t)|$ in the very early stages of elongation reflects the fact that $\sigma(\dot{\epsilon}_0;t)$ increases but the $\Delta n(\dot{\epsilon}_0;t)$ hardly develops in the course of spherulite formation, dominantly because the optical symmetric spherulite may hardly contribute to $\Delta n(\dot{\epsilon}_0;t)$ unless it has been significantly deformed as seen in Figures 6, 8, and 10. Beyond $\sigma(\dot{\epsilon}_0;t) = 1$ MPa, $|C(\dot{\epsilon}_0;t)|$ exhibits an almost constant value ($\cong 0.5 \times 10^{-8}$ Pa^{-1}).

References and Notes

(1) Kotaka, T.; Kojima, A.; Okamoto, M. *Rheol. Acta* **1997**, *36*, 646.
(2) Okamoto, M.; Kubo, H.; Kotaka, T. *Polymer* **1998**, *39*, 3135.
(3) Kubo, H.; Sato, H.; Okamoto, M.; Kotaka, T. *Polymer* **1998**, *39*, 501.
(4) Kubo, H.; Okamoto, M.; Kotaka, T. *Polymer* **1998**, *39*, 4827.
(5) Okamoto, M.; Kubo, H.; Kotaka, T. *Macromolecules* **1998**, *31*, 4223.
(6) Jabarin, S. A. *Polym. Eng. Sci.* **1992**, *32*, 1341.
(7) Salem, D. R. *Polymer* **1994**, *35*, 771.
(8) Lorentz, G.; Tassin, J. F. *Polymer* **1994**, *35*, 3200.
(9) Ishihara, N.; Seimiya, T.; Kuramoto, M.; Uoi, M. *Macromolecules* **1986**, *19*, 2464.
(10) Greis, O.; Xu, Y.; Asano, T.; Petermann, J. *Polymer* **1989**, *30*, 590.
(11) Chatani, Y.; Simane, Y.; Ijitsu, T.; Yukinari, T. *Polymer* **1993**, *34*, 1625.
(12) Chatani, Y.; Simane, Y.; Inagaki, T.; Ijitsu, T.; Yukinari, T.; Shikuma, H. *Polymer* **1993**, *34*, 1620.
(13) Reynolds, N. M.; Hsu, S. L. *Macromolecules* **1990**, *23*, 3463.
(14) Rastogi, S.; Gupta, V. D. *J. Macromol. Sci., Phys.* **1994**, *B33*, 129.
(15) Kobayashi, M.; Nakaoki, T.; Ishihara, N. *Macromolecules* **1989**, *22*, 4377.
(16) Musto, P.; Tavone, S.; Guerra, G.; de Rosa, C. *J. Polym. Sci., Polym. Phys. Ed.* **1997**, *35*, 1055.
(17) Ulcer, Y.; Cakmak, M.; Miao, J.; Hsiung, C. M. *J. Appl. Polym. Sci.* **1996**, *60*, 669.
(18) Meissner, J.; Hostettler, J. *Rheologica Acta* **1994**, *33*, 1.
(19) Wunderlich, B.; Jin, Y.; Boller, A. *Thermochim. Acta* **1994**, *238*, 277.
(20) Gianotti, G.; Valvassori, A. *Polymer* **1990**, *31*, 473.
(21) Suehiro, S. *Nikkei Electron.* **1986**, *936*, 213.
(22) Okamoto, M.; Inoue, T. *Polymer* **1995**, *36*, 2739.
(23) Okamoto, M.; Shinoda, Y.; Kinami, N.; Okuyama, T. *J. Appl. Polym. Sci.* **1995**, *57*, 1055.
(24) Koberstein, J.; Russel, T. P.; Stein, R. S. *J. Polym. Sci., Polym. Phys. Ed.* **1979**, *17*, 1719.
(25) Suzuki, T.; Kovacs, A. J. *Polym. J.* **1970**, *1*, 82.
(26) Larson, R. G. *J. Rheol.* **1984**, *28*, 545.
(27) Yau, W.; Stein, R. S. *J. Polym. Sci.* **1968**, *A2−6*, 1.
(28) Gvozdic, N. V.; Meier, D. J. *Polymer* **1991**, *32*, 493.
(29) Buchner, S.; Wiswe, D.; Zachmann, H. D. *Polymer* **1989**, *30*, 480.
(30) Janeschitz-Kriegel, H. *Polymer Melt Rheology and Flow Birefringence*; Springer-Verlag: Berlin, 1983.
(31) Doi, M.; Edwards, S. F. *The Theory of Polymer Dynamics*; Clarendon Press: Oxford, England, 1986; pp 221−222.
(32) Treloar, L. R. G. In *Die Physik Der Hochpolymeren*; Stuart, H. A., Ed.; Springer-Verlag: Berlin, 1956; Chapter 4.
(33) Treloar, L. R. G. *The Physics of Rubber Elasticity*, 3rd ed.; Clarendon Press: Oxford, England, 1975.
(34) Ryu, D. S.; Inoue, T.; Osaki, K. *Abstract of the 8th Japanese Society of Rheology Symposium on Polymer Processing Technologies*, Nagoya, Japan, 1997; pp 61−62.

MA990186Q